Permian-Triassic mass extinction pulses driven by major marine carbon cycle perturbations

Hana Jurikova[1,2*], Marcus Gutjahr[1], Klaus Wallmann[1], Sascha Flögel[1], Volker Liebetrau[1], Renato Posenato[3], Lucia Angiolini[4], Claudio Garbelli[3], Uwe Brand[5], Michael Wiedenbeck[2], and Anton Eisenhauer[1]

[1]GEOMAR Helmholtz-Zentrum für Ozeanforschung Kiel, Wischhofstr. 1–3, 24148 Kiel, Germany

[2]GFZ Deutsches GeoForschungsZentrum – Helmholtz Zentrum Potsdam, Telegrafenberg, 14473 Potsdam, Germany

[3]Dipartimento di Fisica e Scienze della Terra, Università di Ferrara, Polo Scientifico-tecnologico, Via Saragat 1, 44100 Ferrara, Italy

[4]Dipartimento di Scienze della Terra, Via Mangiagalli 34, Università di Milano, 20133 Milan, Italy

[5]Department of Earth Sciences, Brock University, 1812 Sir Isaac Brock Way, St. Catharines, Ontario L2S 3A1, Canada

*Present address: University of St Andrews, School of Earth and Environmental Sciences, St Andrews KY16 9AL, United Kingdom (hj43@st-andrews.ac.uk)

The Permian-Triassic boundary approximately 251.9 million years ago marked the most severe environmental crisis identified in the geological record that dictated the onwards course for the evolution of life. Magmatism from Siberian Traps is thought to have played a significant role, but the causational trigger and

its feedbacks are yet to be fully understood. Here, we present a new boron isotope-derived seawater pH record from fossil brachiopod shells deposited on the Tethys shelf that demonstrates a substantial decline in seawater pH coeval with the onset of the mass extinction in the latest Permian. Combined with carbon isotope data, our results are integrated in a geochemical model that resolves the carbon cycle dynamics as well as ocean redox conditions and nitrogen isotope turnover. We find that the initial ocean acidification was intimately linked to a large pulse of carbon degassing from the Siberian sill intrusions. We unravel the consequences of the greenhouse effect on the marine environment, and show how elevated sea surface temperatures, export production and nutrient input driven by increased rates of chemical weathering gave rise to widespread de-oxygenation and sporadic sulphide poisoning of the oceans in the earliest Triassic. Our findings enable us to assemble a consistent biogeochemical reconstruction of the mechanisms resulting in the largest Phanerozoic mass extinction.

Current lines of evidence point to a rather rapid catastrophe (~61 ± 48 thousands of years, ka)[1] linked to greenhouse gas emissions from the Siberian Traps large igneous province (LIP)[2,3,4]. The magmatism apparently induced a lethal combination of a substantial input of relatively light carbon to the atmosphere[4,5], increase in global sea surface temperature[6,7,8,9,10], sporadic to widespread anoxia[11,12,13] or euxinia[14,15], and ocean acidification[16,17,18]. The exact causes and consequences, however, remain controversial, and a coherent unifying scenario for the environmental evolution over this important interval in Earth's history is still lacking. To reconstruct the carbon cycle dynamics, we generated a new record of ocean pH for the Permian-Triassic boundary (PTB) using boron isotopes (a well-established proxy for ambient seawater

pH)[19,20,21,22,23] paired with carbon and oxygen isotope data. Our records are assimilated into a box model, which enables us to simulate the carbon release and turnover, and study its effects on the Earth's system – a critical exercise for untangling the driving mechanisms of the extinction, as well as for improving our overall understanding of Earth's climatic and ecological sensitivities.

Boron isotope record of Tethys ocean acidification

We generated high-resolution boron ($\delta^{11}B$), carbon ($\delta^{13}C$) and oxygen ($\delta^{18}O$) isotope records from pristine fossil brachiopod shells[7] composed of low-magnesium calcite (Fig. 1; Methods and Supplement). Our records are based on samples from three stratigraphically well-characterized sections[24] in the Southern Alps of northern Italy – Sass de Putia, Tesero and Val Brutta – where the comparatively uncondensed sedimentary sequences enable a chronologically well-resolved exploration of Tethys Ocean conditions at the PTB (Fig. 1a). This interval covers the global negative carbon isotope excursion (CIE), a characteristic feature of the PTB, associated with major biotic and environmental changes. In addition, several brachiopod specimens from a distant Shangsi section in South China[18] were analysed for comparison. Due to limited sample availability, the Shangsi record does not overlap with that from the Southern Alps; albeit a precise stratigraphic correlation at such high-resolution between the two sites is rather complicated. Nevertheless, the critical decline in $\delta^{11}B$ values, as well as $\delta^{13}C$ and $\delta^{18}O$, following the CIE is registered by brachiopod shells from both South China and Southern Alps, lending strong support to our records and that these are representative of Tethys-wide conditions.

The preservation of original chemical signals in the samples and potential influences

from matrix contamination were thoroughly inspected using a wide suite of pre-screening routines, including minor and trace element analyses (Extended Data Fig. 1; Methods and Supplement). The latter showed that the composition of our samples is broadly consistent with those expected for modern brachiopod species. In several samples though, increased Al/Ca values were detected that are not compatible with primary Al incorporation into the crystal lattice, and may be indicative of sample contamination from clay sediments from the enclosing matrix. These high Al/Ca values, however, did not translate into systematically enriched B/Ca or reduced $\delta^{11}B$; the general trend in our $\delta^{11}B$ record can be reconstructed solely from samples with low Al/Ca values (Extended Data Fig. 2). In addition, the integrity of our $\delta^{11}B$ compositions was cross-checked by combining solution-based and secondary ion mass spectrometry (SIMS) analyses on selected key specimens. The *in situ* nature of the SIMS approach allows for direct $\delta^{11}B$ measurements within specific shell structures, providing further supporting evidence that our $\delta^{11}B$ record was not significantly affected by secondary impurities or post-depositional alterations.

The CIE in the Southern Alps in excess of −4.5 ‰ (Fig. 1c) is accompanied by a decrease in $\delta^{11}B$ values of more than −1.5 ‰ (Fig. 1b) within some 20 ka of the latest Permian (see also Extended Data Fig. 3). This is also closely reflected by a declining $\delta^{18}O$ trend (Fig. 1d), suggesting a dramatic increase in seawater temperatures. Following the CIE, comparably low $\delta^{11}B$, $\delta^{13}C$ and $\delta^{18}O$ values are also found in South China (Fig. 1). We do not observe a recovery to pre-event isotope values after the boundary and into the earliest Triassic. Given the pH-dependent incorporation of $\delta^{11}B$ into biogenic calcite, a substantial suppression of ocean pH accompanying the CIE is evident from our $\delta^{11}B$ data alone. For a quantitative estimate, we convert the $\delta^{11}B$

record to pH considering different $\delta^{11}B$ to pH relationships and ambient seawater $\delta^{11}B$ scenarios ($\delta^{11}B_{sw}$; Methods). Our preferred scenario accounts for biological 'vital effects' on the incorporation of boron into brachiopod calcite, however, in addition we also consider an alternative scenario based on aqueous borate ion relationship (Extended Data Fig. 3). While the first scenario (hereinafter 'standard case scenario') assumes that the $\delta^{11}B$-pH dependency of brachiopod shells is influenced by their internal regulating processes, the second scenario (hereinafter 'borate ion scenario') considers boron incorporation following the inorganic $\delta^{11}B$-pH relationship, and hence the lack of vital effects. These two scenarios effectively envelop the plausible $\delta^{11}B$-pH relationships of brachiopod shells[23]. Had ancient brachiopods potentially higher degrees of vital effects, the $\delta^{11}B$ drop in our record would likely translate to an even more extreme acidification scenario, due to the stronger internal pH regulation and resulting dampened sensitivity to ambient seawater pH. The calibration choice is detailed in the Methods section, and further discussion of vital effects including a pH and model reconstruction considering the alternative 'borate ion scenario' are available in the Supplement. We anchor our initial, pre-CIE $\delta^{11}B$-derived surface ocean pH to plausible pre-event conditions based on previous estimates and our model output. Our $\delta^{11}B$ record then predicts the timing and the magnitude of pH fluctuation with respect to the unperturbed starting conditions prior to the mass extinction event. We find, for the first time, a considerable drop of ~0.5 units in ocean pH at the onset of the extinction in the latest Permian that persists into the earliest Triassic (Fig. 2c).

Carbon release impact on redox and nutrient feedbacks

To characterise the associated carbon release and its impact on the environment, we assimilate the carbon isotope and pH data into a geochemical box model (Methods; see

126 also Extended Data Figs. 4 and 5). The magnitude, dynamics, as well as the most
127 realistic time-resolved $\delta^{13}C$ composition of emitted CO_2 over the PTB is estimated by
128 fitting the model to the data. In addition to our brachiopod data, we consider numerous
129 PTB $\delta^{13}C$ bulk carbonate ($\delta^{13}C_{carb}$; Fig. 2d) as well as organic carbon isotope records
130 ($\delta^{13}C_{org}$; Fig. 2f), comprising different geographical locations and CIE magnitudes,
131 thereby assuring global representation. Our resulting degassing flux (Fig. 2a) amounts
132 to 8800×10^{12} mol CO_2 (106 Pg C, petagram = 1×10^{15} g) over the modelled duration
133 of 1 Ma (–500 ka to 500 ka relative to the CIE). A total amount of ~800×10^{12} mol CO_2
134 (9.6 Pg C) with mantle signature (−6 ‰) is initially released until –35 ka before the
135 CIE. Subsequently, the model diagnoses the emission of ~8000×10^{12} mol CO_2 (96 Pg
136 C) of isotopically substantially lighter CO_2 (−18 ‰). These low $\delta^{13}C$ values reflect the
137 metamorphic degassing of organic carbon during volcanic intrusions into coal basin
138 sediments and are required to match our pH and $\delta^{13}C$ constraints (Fig. 2b). Our outlined
139 emission scenario explains the CIE excursion without invoking light $\delta^{13}C$ signal from
140 methane clathrates. The LIP carbon budget implied by our model is also broadly
141 consistent with other independent estimates and field data[2,3,4] (Supplement).
142 Interestingly, the emitted $\delta^{13}C$ signatures and their temporal resolution are also
143 comparable with volcanic degassing processes from the North Atlantic Igneous
144 Province during the Palaeocene-Eocene Thermal Maximum (PETM)[21] some 56 Ma
145 ago, although the involved carbon budget for the PTB is nearly an order of magnitude
146 greater (106 Pg C as opposed to 12.2 Pg C during the PETM).
147
148 Using a new redox-resolving ocean model[25] we determine the ensuing series of changes
149 in the ocean chemistry (Fig. 2 and Fig. 3). We find that degassing from the Siberian
150 Traps leads to a steep increase in atmospheric pCO_2, even though a large fraction of the

151 emitted CO_2 is dissolved in the surface ocean, transferred into depth via a gradual
152 increase in export production, and rapidly consumed and converted into bicarbonate via
153 enhanced silicate and carbonate weathering (Fig. 2). Initially, the partial pressure of
154 CO_2 in the atmosphere is relatively low in the Late Permian (~500 to ~800 ppm, *sensu*
155 *stricto* vppm; Fig. 2e). Following the CIE, at the onset of the extinction CO_2 levels rise
156 abruptly peaking at 44 ka (up to max. 4400 ppm), and remain elevated (~1500 ppm)
157 throughout the Early Triassic, consistent with previous palaeo-pCO_2
158 estimates[5,26,27,28,29]. The sharp increase in CO_2 imposes a lasting disruption to the
159 marine carbonate cycle, prompting a severe decline in surface ocean pH (Fig. 2c),
160 which only partially recovers during the Early Triassic. In response to the carbon
161 emission, our model predicts warming by almost 10 °C (Fig. 2h) in agreement with
162 proxy-based evidence[6,30,31]. Rates of chemical weathering strongly increase (Fig. 2g),
163 as does marine export production (Fig. 2i) and nutrient input, which is congruent with
164 the increase in detrital fluxes to the global ocean observed in numerous sedimentary
165 PTB records[32].
166
167 Dissolved oxygen concentrations (Fig. 3a) in sub-surface waters decline abruptly soon
168 after the CIE and remain low over the Early Triassic due to the increase in export
169 production and respiration. The surface ocean remains oxygenated through exchange
170 with the atmosphere. Dissolved nitrate (Fig. 3b) sharply increases with the CIE,
171 promoted by a rise in sea surface temperatures (SSTs) and temperature-dependent
172 nitrogen fixation, but it declines again with a coeval increase in pelagic and benthic
173 denitrification brought on by the spread of low-oxygen conditions. Complete depletion
174 of oxygen and nitrate is only attained in the intermediate waters of the Tethys where it
175 results in an accumulation of dissolved sulphide (Fig. 2f). Under the post-PTB low-

176 oxygen conditions, ammonium (Fig. 3c), phosphate (Fig. 3d) and iron (Fig. 3e) are
177 released from seabed sediments into the overlying water column and support the rise in
178 export production and respiration in a strong positive feedback loop.
179
180 We further extend our model to simulate the turnover of stable nitrogen isotopes ($\delta^{15}N$;
181 Supplement), which reflect the composition of marine organic matter formed in the
182 surface ocean (Fig. 3h). The initial $\delta^{15}N$ decline following the CIE is linked to a rapid
183 rise in nitrogen fixation, but subsequently $\delta^{15}N$ increases due to pelagic denitrification
184 that consumes a large portion of the dissolved nitrate pool in sub-surface waters,
185 preferentially removing the light isotope (Fig. 3g). Following the consumption of the
186 excess nitrate, $\delta^{15}N$ declines again as a result of ongoing nitrogen fixation. Due to the
187 strong denitrification under low oxygen conditions, modelled plankton growth is
188 largely limited by nitrate, while nitrogen fixation is limited by phosphate. Although we
189 acknowledge that the $\delta^{15}N$ model fit, in particular close to the PTB, is less reliable due
190 to the large scatter in the data, the modelled changes explain the overall low $\delta^{15}N$ values
191 in the Early Triassic relative to the Late Permian, a feature reported from numerous
192 sedimentary records[33,34]. This advocates for high SST and increase in the riverine
193 phosphate flux to the ocean induced by enhanced weathering and erosion as triggers of
194 the observed rise in nitrogen fixation and productivity after the PTB.
195
196 The increase in global productivity along with the depletion of dissolved oxygen
197 simulated by our redox-resolving model is consistent with data-based reconstructions.
198 Accumulation rates of organic carbon and barite determined in numerous sediment
199 cores from the Tethys and Panthalassa indicate a significant increase in export
200 production from the latest Permian into the Early Triassic[32,35]. Marine plankton

communities underwent drastic restructuring over the PTB with warming and loss of oxygen fostering the proliferation of prokaryotic cyanobacteria over eukaryotic algae[35], which is consistent with the increase in nitrogen fixation predicted by the model. Global loss of oxygen across the PTB has been documented by $\delta^{238}U$ and Th/U records from the Tethys and Panthalassa indicating wide-spread uranium uptake in sediments after the PTB[11,12,13]. Conditions where oxygen and nitrate rather than sulphate are used as terminal electron acceptors for organic matter degradation are also characteristic of modern oxygen minimum zones[36] and lead to uranium accumulation in marine sediments[37]. Evidence for euxinic conditions, where sulphide dissolved in shallow intermediate waters is transported to the euphotic zone has been reported from biomarker studies[15].

The carbon cycle perturbations culminate at about 100 ka after the CIE with waning LIP emissions, although neither the atmospheric pCO_2 nor the marine biogeochemical cycles return to pre-event conditions during the Early Triassic (Fig. 2 and Fig. 3). LIP-CO_2 is converted into seawater alkalinity via enhanced chemical weathering. Upsurge of export production aids the drawdown of atmospheric pCO_2, and the ocean pH recovery is additionally augmented by alkalinity production (Fig. 2k) during denitrification under suboxic conditions. Neritic carbonate burial initially declines following the CIE due to strong acidification of surface waters, but increases after the PTB in response to an increase in alkalinity (Fig. 2j). Since calcifying phytoplankton emerged only later in the Mesozoic, pelagic carbonates were absent during this time and carbonate burial may have only occurred on the shelf. Under such conditions, carbonate compensation would be less efficient than in the modern ocean and could have led to strong calcite oversaturation of surface waters[38] (Fig. 2l). Our model

calculations are also in line with carbonate burial rates derived from strontium and calcium isotope records across the PTB[39,40], and geologic evidence of unusually high abiotic calcium carbonate precipitation in the Early Triassic[41]. The marine crisis, however, persists through the Early Triassic, due to the delayed recovery of the redox state. We note that the evolution of the surface ocean pH and the transition to suboxic conditions is heavily dependent on the initial oxidation state of the ocean as shown by additional model simulations and sensitivity tests (Supplement). For instance, an increase or decrease of 50% in riverine phosphate input leads to substantial changes in export production and nitrogen fixation, and thereby the corresponding drawdown of atmospheric pCO_2. Yet these simulations fail to reproduce the proxy-based evidence, such as the $\delta^{13}C$, pH or $\delta^{15}N$ records, making a strong argument in favour of the 'standard case scenario' presented here.

Global consequences for the marine ecosystem

These findings lead us to view the PTB mass extinction as a cascading marine collapse, triggered by a multi-millennial-scale voluminous injection of carbon to the atmosphere by the emplacement of Siberian Traps sill intrusions[2,42]. Its magnitude profoundly altered the biogeochemical processes, setting off a chain of events that selectively eliminated different groups of marine organisms[43]. In the latest Permian, the CO_2 greenhouse effect resulted in strong heating and acidification of the surface ocean, which prompted the initial disappearance of all reef-building taxa[44,45]. Experiments on modern organisms[46] indicate that an increase in pCO_2 alone is generally insufficient to severely impair marine calcification. It is the synergic effect of acidification and rising temperatures that is detrimental, and which presumably was lethal to ancient biota. The subsequent extinction pulse followed in the earliest Triassic, with a strong positive

redox feedback driving the deoxygenation of sub-surface waters. Both our 'standard model scenario' as well as further sensitivity tests (Supplement) suggest that the deep ocean remained in a depleted oxygen state but was not seriously affected by sulphide poisoning. Sulphide formation may have, however, reached toxic levels along the Tethys' continental margins and in upwelling regions of Panthalassa, where low oxygen and high nutrient concentrations in ascending sub-surface waters could have promoted anoxic and/or euxinic conditions, aggravating the environmental crisis. The protracted recovery from suboxic conditions, nitrate limitation, possibly amplified by spreading anoxia or sulphide poisoning, would have preferentially wiped out the non-motile and physiologically unbuffered taxa[43]. Together, the distinct stressors led to a physiological crisis accompanied by a dramatic shrinking of the habitable realm, limiting the marine refuge to a narrow zone in the upper water column[24,47].

Considering the vastly differing timescales and carbon budgets involved LIP carbon cycle dynamics is a poor analogy for present-day fossil fuel emissions, notwithstanding that, the modern geologic carbon reservoirs are insufficient for anthropogenic release beyond centennial time scales. It is, however, noteworthy that even the peak emissions rate during the largest known mass extinction (58×10^{12} mol CO_2 or 0.7 Pg C per year) is still more than 14 times less than the current anthropogenic rate (9.9 ± 0.5 Pg C per year)[48]. The environmental deterioration during the PTB took several thousands of years to unfold, whereas the current, unprecedented emissions rate already has started to take a toll on the marine ecosystems[49]. A coupled increase in atmospheric pCO_2 and a decrease in surface ocean pH[49], global warming, changes in productivity as well as oxygen depletion[50] have been reported world-wide, suggesting that the scenario

outlined here for the PTB may also be relevant for understanding future environmental and climatic trends.

277 **References**

278

279 1. Burgess, S.D., Bowring, S. & Shen, S.-Z. High-precision timeline for Earth's
280 most severe extinction. *Proc. Natl. Acad. Sci*. **111**, 3316–3321 (2014).

281

282 2. Svensen, H. *et al.* Siberian gas venting and the end-Permian environmental
283 crisis. *Earth Planet. Sci. Lett.* **277**, 490–500 (2009).

284

285 3. Burgess, S.D. & Bowring, S.A. High-precision geochronology confirms
286 voluminous magmatism before, during, and after Earth's most severe extinction.
287 *Sci. Adv.* **1**, 14 (2015).

288

289 4. Saunders, A.D. Two LIPs and two Earth-system crises: the impact of the North
290 Atlantic Igneous Province and the Siberian Traps on the Earth-surface carbon
291 cycle. *Geol. Mag*. **153**, 201–222 (2016).

292

293 5. Cui, Y. & Kump, L.R. Global warming and the end-Permian extinction event:
294 Proxy and modeling perspectives. *Earth-Sci. Rev.* **149**, 5–22 (2015).

295

296 6. Sun, Y. *et al.* Lethally hot temperatures during the early Triassic greenhouse.
297 *Science* **338**, 366–370 (2012).

298

299 7. Brand, U. *et al.* The end-Permian mass extinction: A rapid volcanic CO_2 and
300 CH_4-climatic catastrophe. *Chem. Geol.* **323**, 121−144 (2012).

301

8. Winguth, A.M.E., Shields, C.A. & Winguth, C. Transition into a Hothouse World at the Permian-Triassic boundary-A model study. *Palaeogeogr. Palaeoclimatol. Palaeoecol.* **440**, 316−327 (2015).

9. Garbelli C., *et al.* Neotethys seawater chemistry and temperature at the dawn of the end-Permian mass extinction. *Gondwana Res.* **35**, 272−2 (2016).

10. Wang., W. *et al.* A high-resolution Middle to Late Permian paleotemperature curve reconstructed using oxygen isotopes of well-preserved brachiopod shells, *Earth Planet. Sci. Lett.* **540**, 116245 (2020).

11. Lau, K.V. *et al.* Marine anoxia and delayed Earth system recovery after the end-Permian extinction. *Proc. Natl. Acad. Sci*. **113**, 2360–2365 (2016).

12. Elrick, M. *et al.* Global-ocean redox variation during the middle-late Permian through Early Triassic based on uranium isotope and Th/U trends of marine carbonates. *Geology* **45**, 163–166 (2017).

13. Zhang, F.F. *et al.* Congruent Permian-Triassic $\delta^{238}U$ records at Panthalassic and Tethyan sites: Confirmation of global-oceanic anoxia and validation of the U-isotope paleoredox proxy. *Geology* **46**, 327–330 (2018).

14. Korte, C. *et al.* Carbon, sulfur, oxygen and strontium isotope records, organic geochemistry and biostratigraphy across the Permian/Triassic boundary in Abadeh, Iran. *Int. J. Earth Sci.* **93**, 565–581 (2004).

15. Grice, K. *et al.* Photic zone euxinia during the Permian-Triassic superanoxic event. *Science* **307**, 706–709 (2005).

16. Payne, J.L. *et al.* Calcium isotope constraints on the end-Permian mass extinction. *Proc. Natl. Acad. Sci*. **107**, 8543−8548 (2010).

17. Clarkson, M.O. *et al.* Ocean acidification and the Permo-Triassic mass extinction. *Science* **348**, 229−232 (2015).

18. Garbelli, C., Angiolini, L. & Shen, S.-Z. Biomineralization and global change: A new perspective for understanding the end-Permian extinction. *Geology* **45**, 19−22 (2017).

19. Hönisch, B., Hemming, N.G., Archer, D., Siddall, M. & McManus, J.F. Atmospheric Carbon Dioxide Concentration Across the Mid-Pleistocene Transition. *Science* **324**, 1551−1554 (2009).

20. Rae, J.W.B. *et al.* CO_2 storage and release in the deep Southern Ocean on millennial to centennial timescales. *Nature* **562**, 569−573 (2018).

21. Gutjahr, M. *et al.* Very larger release of mostly volcanic carbon during the Palaeocene-Eocene Thermal Maximum. *Nature* **548**, 573−577 (2017).

22. Henehan, M. *et al.* Rapid ocean acidification and protracted Earth system

recovery followed the end-Cretaceous Chicxulub impact. *Proc. Natl. Acad. Sci.* **116**, 22500–22504 (2019).

23. Müller, T. *et al.* Ocean acidification during the early Toarcian extinction event: Evidence from boron isotopes in brachiopods. Geology, *in press* https://doi.org/10.1130/G47781.1 (2020).

24. Posenato, R. Survival patterns of microbenthic marine assemblages during the end-Permian mass extinction in the western Tethys (Dolomites, Italy). *Palaeogeogr. Palaeoclimatol. Palaeoecol.* **280**, 150–167 (2019).

25. Wallmann, K. *et al.* Periodic changes in the Cretaceous ocean and climate caused by marine redox see-saw. *Nat. Geosci.* **12**, 456–462 (2019).

26. Retallack, G. J. A 300-million-year record of atmospheric carbon dioxide from fossil plant cuticles. *Nature* **411**, 287−290 (2001).

27. Goddéris, Y. *et al.* Causal or casual link between the rise of nannoplankton calcification and a tectonically-driven massive decrease in Late Triassic atmospheric CO_2? *Earth Planet. Sci. Lett.* **267**, 247−255 (2008).

28. McElwain, J. C., Wagner, P. J. & Hesselbo, S. P. Fossil Plant Relative Abundances Indicate Sudden Loss of Late Triassic Biodiversity in East Greenland. *Science* **324**, 1554−1556, 2009.

29. Witkowski, C. R., Weijers, J. W. H., Blais, B., Schouten, S. & Damste, J. S. S. Molecular fossils from phytoplankton reveal secular P_{CO2} trend over the Phanerozoic. *Sci. Adv.* **4**, 7 (2018).

30. Joachimski, M. M. *et al.* Climate warming in the latest Permian and the Permian-Triassic mass extinction. *Geology* **40**, 195−198 (2012).

31. Schobben, M., Joachimski, M. M., Korn, D., Leda, L. & Korte, C. Palaeotethys seawater temperature rise and an intensified hydrological cycle following the end-Permian mass extinction. *Gondwana Res.* **26**, 675−683 (2014).

32. Algeo, T.J. *et al.* Plankton and productivity during the Permian-Triassic boundary crisis: An analysis of organic carbon fluxes. *Glob. Planet. Change* **105**, 52–67 (2013).

33. Saitoh, M. *et al.* Nitrogen isotope chemostratigraphy across the Permian-Triassic boundary at Chaotian, Sichuan, South China. *J. Asian Earth Sci.* **93**, 113−128 (2014).

34. Sun, Y. D. *et al.* Ammonium ocean following the end-Permian mass extinction. *Earth Planet Sci. Lett.* **518**, 211−222 (2019).

35. Shen, J. *et al.* Marine productivity changes during the end-Permian crisis and Early Triassic recovery. *Earth-Sci. Rev.* **149**, 136–162 (2015).

402 36. Canfield, D. E. Models of oxic respiration, denitrification and sulfate reduction
403 in zones of coastal upwelling. *Geochim. Cosmochim. Acta* **70**, 5753−5765
404 (2006).
405
406 37. Anderson, R. F. *et al.* Deep-Sea Oxygen Depletion and Ocean Carbon
407 Sequestration During the Last Ice Age. *Glob. Biogeochem. Cy.* **33**, 301−317
408 (2019).
409
410 38. Zeebe, R. & Westbroek, P. A simple model for the $CaCO_3$ saturation state of
411 the ocean: The "Strangelove", the "Neritan", and the "Cretan" Ocean. *Geochem.*
412 *Geophy. Geosy.* **4**, 1104 (2003).
413
414 39. Vollstaedt, H. *et al.* The Phanerozoic $d^{88/86}Sr$ record of seawater: New
415 constraints on past changes in oceanic carbonate fluxes. *Geochim. Cosmochim.*
416 *Acta* **128**, 249–265 (2014).
417
418 40. Silva-Tamayo, J. C. *et al.* Global perturbation of the marine calcium cycle
419 during the Permian-Triassic transition. *Geol. Soc. Am. Bull.* **130**, 1323−1338
420 (2018).
421
422 41. Woods, A. Assessing Early Triassic paleoceanographic conditions via unusual
423 sedimentary fabrics and features. *Earth Sci. Rev.* **137**, 6−18 (2014).
424

42. Burgess, S.D., Muirhead, J.D. & Bowring, S.A. Initial pulse of Siberian Traps sills as the trigger of the end-Permian mass extinction. *Nat. Commun.* **8**, 164 (2017).

43. Song, H.J., Wignall, P.B., Tong, J.N. & Yin, H.F. Two pulses of extinction during the Permian-Triassic crisis. *Nat. Geosci.* **6**, 52–56 (2013).

44. Brayard, A. *et al.* Transient metazoan reefs in the aftermath of the end-Permian mass extinction. *Nat. Geosci.* **4**, 693–697 (2011).

45. Martindale, R.C., Foster, W.J. & Velledits, F. The survival, recovery, and diversification of metazoan reef ecosystems following the end-Permian mass extinction event. *Palaeogeogr. Palaeoclimatol. Palaeoecol.* **513**, 100–115 (2019).

46. Reynaud, S., *et al*. Interacting effects of CO_2 partial pressure and temperature on photosynthesis and calcification in a scleractinian coral. *Glob. Chang. Biol.* **9**, 1660−1668 (2003).

47. Beatty, T.W., Zonneveld, J.-P. & Henderson, C.M. Anomalously diverse Early Triassic ichnofossil assemblages in northwest Pangea: A case for shallow-marine habitable zone. *Geology* **36**, 771−774 (2008).

48. Le Quéré, C. *et al*. Global Carbon Budget 2018. *Earth Syst. Sci. Data* **10**, 2141−2194 (2018).

450

451 49. Orr, J.C. *et al.* Anthropogenic ocean acidification over the twenty-first century

452 and its imapact on calcifying organisms. *Nature* **437**, 681–686 (2005).

453

454 50. Schmidtko, S., Stramma, L. & Visbeck, M. Decline in global oxygen content

455 during the past five decades. *Nature* **542**, 335–339 (2017).

456 **Correspondence and requests for materials** should be addressed to H.J. (hj43@st-
457 andrews.ac.uk).
458
459 **Acknowledgements**
460 This project has received funding from the European Union's Horizon 2020 research
461 and innovation programme under the Marie Sklodowska-Curie grant agreement No.
462 643084 (BASE-LiNE Earth). K.W. was supported by the HGF (ESM project), and S.F.
463 by the DFG (SFB 754, sub-project A7). L.A. and R.P. were supported by the MURST
464 (PRIN 2017RX9XXXY, project 'Biota resilience to global change: biomineralization
465 of planktic and benthic calcifiers in the past, present and future'). We thank Dirk
466 Nürnberg for help with carbon and oxygen isotope analyses, and Ana Kolevica and
467 Tyler Goepfert for laboratory support (at the GEOMAR Helmholtz Centre for Ocean
468 Research in Kiel). We are grateful to Frédéric Couffignal and Alexander Rocholl for
469 assistance with SIMS analyses, Uwe Dittmann for sample preparation, and Ilona
470 Schäpan for SEM imaging (at the GFZ German Research Centre for Geosciences −
471 Helmholtz Centre in Potsdam). Special thanks to Arne Winguth (at the University of
472 Texas Arlington) for providing us the model output.
473
474 **Author contributions**
475 H.J., M.G., V.L., and A.E. developed the concept and designed the study. H.J. carried
476 out chemical sample preparation as well as elemental and isotopic analyses. M.W.
477 provided isotopic micro-analyses. U.B., R.P., L.A. and C.G. provided and screened the
478 samples. R.P., L.A., C.G. and H.J. developed the age model. K.W. and S.F. devised the
479 box model and performed the analyses. H.J. wrote the manuscript, and all authors

480 discussed the results, contributed to the interpretation of the data and the final
481 manuscript.
482
483 **Competing interests**
484 The authors declare no competing interests.
485
486 **Figure 1. Brachiopod-based stable isotope data from Italy and China. a** Late
487 Permian palaeogeographic reconstruction (Methods) with location of the sampling
488 sites; **b** $\delta^{11}B$; **c** $\delta^{13}C$ and **d** $\delta^{18}O$ record derived from brachiopod shells from Southern
489 Alps (Sass de Putia, Tesero and Val Brutta; BWFB – Bellerophon-Werfen Formation
490 boundary) and South China (Shangsi). Error bars in **a** indicate the analytical uncertainty
491 for solution-based $\delta^{11}B$ (2SD = 0.2 ‰) and SD between multiple ion spots
492 measurements within a single shell for SIMS $\delta^{11}B$. Stratigraphy of the GSSP Meishan
493 is shown for comparison. Purple field marks the onset of the CIE as defined in our age
494 model (see Methods and Supplement), with geochronology based on latest age
495 estimates[1].
496
497 **Figure 2. Modelled marine carbonate system and climate change. a** CO_2 release via
498 Siberian Traps LIP degassing applied as model forcing; **b** isotopic composition of
499 released CO_2; **c** surface pH of Tethys Ocean; **d** carbon isotope composition of
500 carbonates deposited on Tethys shelf (data sources in Supplement); **e** global
501 atmospheric partial presurre CO_2 projected by the carbon cycle model; **f** carbon isotope
502 composition of organic carbon in sediments deposited on Panthalassa seafloor (data
503 sources in Supplement); **g** global rate of silicate (granite + basalt) and carbonate
504 weathering; **h** sea surface temperatures (SSTs) for Tethys and Panthalassa; **i** marine

export production of particulate organic carbon (POC) across 100 m water depth; **j** burial of POC and neritic carbonate on the global shelf; **k** seawater total alkalinity (TA); and **l** saturation state of surface (0–100 m) and deep waters (>1300 m) of Tethys and Panthalassa with respect to calcite.

Figure 3. Modelled redox state of the ocean, dissolved nutrient concentrations and nitrogen cycling. a dissolved oxygen in surface (0–100 m), intermediate (100–1300 m) and deep waters (>1300 m) of Tethys and Panthalassa; **b** dissolved nitrate; **c** dissolved ammonium; **d** dissolved phosphate; **e** total dissolved iron; and **f** total dissolved sulphide; **g** reconstruction of nitrogen cycling in Tethys Ocean; and **h** nitrogen isotope composition of Tethys sediments (data sources are provided in the Supplement).

Methods

Site and sample information

We selected fossil brachiopods from well-constrained successions of the eastern Southern Alps (Sass de Putia, Tesero and Val Brutta in Italy; ref. 51 for an overview) and Shangsi (China)[18] spanning the Permian-Triassic boundary (PTB) interval. We opted for this novel archive approach for two particular reasons; firstly because skeletal components of marine calcifiers are the most appropriate boron-based pH-recorders[19,20,21,22,23] and secondly because brachiopod shells are composed of low-magnesium calcite, the most robust polymorph of calcium carbonate to diagenetic alterations. Our records are based on carefully chosen unaltered specimens from a collection[7] that has been extensively pre-screened involving optical and petrographic inspections, scanning electron microscopy (SEM; see also in Supplement), cathodoluminescence (CL), and polarising microscopy alongside criteria based on trace, rare earth and redox sensitive elements to assure microstructural and chemical integrity. Additionally, further related specimens from the collections of Renato Posenato and Lucia Angiolini were used to complement the set, which allowed us to extend the timeline and the resolution of the previous records, and capture the full span of the $\delta^{13}C$ excursion. Brachiopods from these PTB sections are extremely well preserved with discernible internal layers analogous to that in modern brachiopods[7,53,54,55]. The brachiopod taxa from the Southern Alps comprise the genera *Comelicania*, *Comelicothyris*, *Janiceps* and *Orbicoelia* of the Class Rhynchonellata, and *Ombonia* and *Orthothetina* of the Class Strophomenata. To evaluate whether the pH suppression observed in our record from Southern Alps was a Tethys-wide event, we also included selected *Paracrurithyris* (Rhynchonellata) specimens from the distant Shangsi section[18] to the record for a comparison. The age model was based on a stratigraphic correlation to Meishan GSSP and the latest absolute geochronologic dates[1]. Further description of the stratigraphy and our devised age model is available in the Supplement (S1). The palaeogeographic map reconstruction including the extent of the Siberian Traps province was based on geological evidence[56,57].

Sample preparation and geochemical analyses

The inner secondary layer of brachiopod shells is deemed as the most appropriate part for geochemical analyses[58,59] and was carefully sampled using a handheld precision drill (Proxxon) with a mounted dental tip or a carbide pen under a binocular microscope. Approximately 1–5 mg of homogenous calcium carbonate powder was collected in 1.5 ml centrifuge vials. A small fraction of the powder was analysed for $\delta^{13}C$ and $\delta^{18}O$ composition on a Thermo Finnigan MAT252 stable isotope mass spectrometer coupled online to an automated Kiel carbonate preparation line. The rest was measured for elemental content and $\delta^{11}B$ using inductively coupled plasma mass spectrometry on a Quadrupole ICP-MS (Agilent 7500x) and Thermo Scientific Neptune Plus MC-ICP-MS, respectively. Measurements and sample preparation work was carried out at the GEOMAR Helmholtz Centre for Ocean Research Kiel. Purification and the treatment of the samples for elemental and $\delta^{11}B$ analyses was carried out according to previously established protocols[52,60]. The powder material was at first thoroughly cleaned to remove any adhering clays, then oxidatively cleaned using buffered peroxide and finally dissolved in 0.5 M HNO_3. Prior to $\delta^{11}B$ analyses, samples

were additionally screened for chemical consistency by checking various elemental ratios (Al/Ca, B/Ca, Mg/Ca, Sr/Ca, Mn/Ca, Fe/Ca and U/Ca; Extended Data Fig. 1; see also Supplement S2). Although few samples had elevated Al/Ca, similar to observations from previous studies[21], this did not translate into altered $\delta^{11}B$ values, as supported by the good agreement between solution-based and *in situ* SIMS measurements. Likewise, we observed variable B/Ca, Mg/Ca, Sr/Ca, Mn/Ca, Fe/Ca and U/Ca, however, with the exception of few samples, measured values were within the range of recent brachiopods[58] and without significant systematic effect on the $\delta^{11}B$ values. We also underscore that, for most parts, our record is based on several specimens per stratigraphic horizon, with good agreement in $\delta^{11}B$ values between them despite variable Al/Ca or other ratios, implying that any potential source of contamination to the samples had limited impact on the $\delta^{11}B$ values. This is also supported by the very depleted B/Ca, but elevated and variable Al/Ca of the enclosing matrix based on three samples of Late Permian cement (Extended Data Fig. 1), which was the likely source. Ultimately though, as mentioned in the main text, our overall $\delta^{11}B$ trends may still be reconstructed when samples with low Al/Ca only are taken into account. Our total procedural blanks were below <100 pg B ($\delta^{11}B$ ~0–20 ‰) and hence negligible considering the typical sample size of 10–50 ng B. The external reproducibility on $\delta^{11}B$ was ± 0.2 ‰ (2SD) assessed by repeated measurements of purified carbonate standard reference materials measured along with samples and treated identically ($\delta^{11}B$ = 24.51 ± 0.18 ‰, n = 5 for the coral reference material JCp-1; and $\delta^{11}B$ = 15.96 ± 0.21 ‰, n = 16 for our in-house brachiopod standard MVS-1), in line with our previously published results[52]. In addition, *in situ* boron isotope measurements were carried out on selected key specimens using secondary ion mass spectrometry (SIMS). This approach allows for determination of $\delta^{11}B$ values in brachiopod shells directly, without the chemical processing of samples, and with measured isotopic ratios being directly comparable to the solution-based MC-ICP-MS technique[52,61]. SIMS analyses and sample preparation was done at the GFZ German Research Centre for Geosciences – Helmholtz Centre Potsdam. Measurements were performed on a CAMECA 1280-HR SIMS instrument as described in detail in Supplement (S3). In brief, cross-sections of brachiopod shells were embedded in epoxy, polished and coated with gold. We used a $^{16}O^-$ primary beam operated in Köhler illumination with intensity varying between approximately 40 to 60 nA that was focused into an aperture delimited spot of ~30 µm. The analyses were conducted in a multi-collection mode by simultaneously measuring ^{10}B and ^{11}B on electron multipliers. For instrument calibration and reporting of measured isotopic ratios to the common NIST 951 scale we used the inorganic calcite standard reference material UWC-1[62]. The count rate on the $^{11}B^+$ mass station on the UWC-1 was typically in the range 5000 to 10,000 ions/second, which translated to an uncertainty ~1 to 1.5 ‰ (SD) for individual analyses (for the brachiopod samples the count rate was usually at least double that of the UWC-1). The external analytical repeatability based on 82 determinations on the UWC-1 over 4 days of the measurement session was better than ± 1.4 ‰ (SD, n = 82). Results are shown as a mean of multiple ion spot measurements within a single specimen with SD between them.

pH calculation

A prerequisite for the reconstruction of pH from $\delta^{11}B$ values of marine biogenic carbonates is the knowledge of $\delta^{11}B$ composition of seawater ($\delta^{11}B_{sw}$). Boron in seawater is homogenous with a residence time of approximately 11 to 20 Ma, and thus

the $\delta^{11}B_{sw}$ needs to be constrained for the PTB. The $\delta^{11}B_{sw}$ composition of the modern ocean is 39.6 ‰, but was proposed to have been lower in the past (~37 ‰ 60 Ma ago)[63]. Permian $\delta^{11}B_{sw}$ values were previously calculated by modelling of the boron geochemical cycle suggesting $\delta^{11}B_{sw}$ of ~38 ‰ for the Early Permian (Late Sakmarian) and $\delta^{11}B_{sw}$ of ~34‰ for the latest Permian, just prior to the PTB[65]. To provide a further constrain on the $\delta^{11}B_{sw}$, but not obviating previous estimates, we considered a range of values that effectively envelopes the possible $\delta^{11}B_{sw}$, yet allows for the full expression of the proxy. Assuming that boron is incorporated into brachiopod calcite following the inorganic borate ion fractionation[65] with negligible vital effects, the maximum integer $\delta^{11}B_{sw}$ that enables the calculation of pH from all our brachiopod $\delta^{11}B$ values within the dynamic range of the proxy is 38 ‰, with values ≥39 ‰ being beyond the sensitivity of the proxy at the lower pH spectrum. On the other hand, applying a brachiopod calibration that accounts for biological influence on the incorporation of boron[66], the highest feasible integer $\delta^{11}B_{sw}$ is 35 ‰ (similarly, values ≥36 ‰ are beyond the proxy range at the lower pH spectrum). A lower-end limit on the $\delta^{11}B_{sw}$ can be placed by tying our average pre-event brachiopod $\delta^{11}B$ (14 ± 0.5 ‰, 2SD, n = 7; based on the mean composition of brachiopods from beds wPK5 top, wPK6A, and wPK6A base; note that the specimens from beds PK4 are not included due less reliable constrains on their age; see also Supplement S1) to a probable pre-event pH conditions and inversely derive the $\delta^{11}B_{sw}$. Considering that modern ocean mean pH is 8.1, and Late Permian was a high pCO_2 world, but the ocean did not contain a carbonate buffer due to the lack of pelagic carbonate producers, it is reasonable to assume that pre-event pH must have been lower than today. Assuming a mean pre-event pH of ~7.8, based on model-derived constraints of Late Permian pH for a 'Neritan' ocean[67], the $\delta^{11}B_{sw}$ of ~38 ‰ and ~35 ‰ via borate ion fractionation and brachiopod calibration, respectively, may be calculated (in this case higher pre-event pH values would result in lower $\delta^{11}B_{sw}$ estimates). The choice of the pre-event pH value, and hence $\delta^{11}B_{sw}$, can be further supported by additional runs of our geochemical box model when forced not to violate constrains given by LIP degassing and the global $\delta^{13}C$ record (see Supplement S4).

In addition to the $\delta^{11}B_{sw}$, the application of an appropriate archive-specific $\delta^{11}B$ calibration is required in order to calculate pH from $\delta^{11}B$ values. Typically, more recent reconstructions spanning the Neogene employ extant archives (e.g. foraminifera or corals) for which a pH-dependent $\delta^{11}B$ calibration can be made using culture or field studies in order to assess the role of vital effects due to their internal biological processes. This is, however, not possible for any Palaeozoic brachiopods which are extinct and thus such assessments must be made indirectly. Similar to the calculation of $\delta^{11}B_{sw}$, in order to account for different influences on the incorporation of boron into brachiopod shells we consider two different calibrations; the inorganic $\delta^{11}B$-to-pH relationship of aqueous borate ion[65] and a brachiopod calibration bracketing their vital effects[66]. Because vital effects, as in other calcifiers, are also undoubtedly inherent to brachiopods, we chose the pH reconstruction based on brachiopod calibration[66] as our preferred scenario ('standard case scenario'). However, for comparison we also provide a second detailed scenario based on pH values calculated using the borate ion relationship ('borate ion scenario'; Extended Data Fig. 3; and detailed in Supplement S4).

Two further calibrations can be found in the literature; a calibration based on modern terebratellids[68] and a calibration based on cultured *Magellania venosa*[52]. The first one[68] results in pH estimates rather similar to that of the brachiopod calibration of ref. 66. In

comparison, the *M. venosa* calibration[52] results being highly sensitive within the defined $\delta^{11}B_{sw}$ envelope, with only minor $\delta^{11}B$ variations resulting in extreme pH change, which are in most instances beyond the dynamic proxy range. A pH reconstruction is, nonetheless, feasible using the *M. venosa* calibration[52] if $\delta^{11}B_{sw}$ <30 ‰. Such low $\delta^{11}B_{sw}$ values, however, at present appear rather unlikely for the PTB. Hence, while the *M. venosa* calibration appears to be applicable to other recent cold-water species as well, we suspect that it is not suited for Palaeozoic brachiopods. Moreover, many modern terebratellids, and specifically *M. venosa*, thrive in highly dynamic cold-water regimes characteristic of large seasonal variations and as a result likely exhibit stronger vital effects than ancient warm-water dwelling species.

Species-specific vital effects may further complicate the use of one general calibration[68]. To overcome this, and because the use of multiple brachiopod species appears inevitable for providing a PTB record of sufficient temporal resolution, we considered the following measures. First, we strictly limited the number of species used in our record, but in particular brachiopod classes since brachiopods vary mostly at a higher taxonomic level[69]. Second, because vital effects are closely linked to organism's niche, we examined the habitat and morphology parallels between the species used. Finally, we devised the record taking into account stratigraphic overlap between the different species during the pre-event as well as the event conditions, giving us confidence that the final reconstruction is not significantly affected by species-specific offsets. Indeed, the overall $\delta^{11}B$ trend of our full record holds when solely based on one brachiopod group (Rhynchonellata) from one site (Dolomites, N. Italy; Extended Data Fig. 2).

The Late Permian record prior to the CIE is almost exclusively based on *Comelicania* sp., but also includes two specimens of *Janiceps* sp. (both Rhynchonellata), which show a close agreement, not larger than typical intraspecific variations among different *Comelicania* sp. shells. Just after the CIE, the record still includes several *Comelicania* sp., but also few other species belonging to both Rhynchonellata and Strophomenata. Note that bed wPK11B (app. 7 ka relative to the CIE) comprises *Janiceps* sp. and *Comelicothyris* sp. (both Rhynchonellata) as well as *Ombonia* sp. (Strophomenata) specimens, which show highly similar $\delta^{11}B$ values (13.18 ± 0.48, SD between specimens, n = 6), further supporting the fact that interspecific variations, even at a class level, are minimal and do not significantly impact our $\delta^{11}B$ values. The latest part of our record documenting acidification, despite the scarcity of brachiopods in these beds, is based on both brachiopod classes with multiple specimens of *Orbicoelia* sp. (Rhynchonellata) and *Teserina* sp. (Strophomenata) from northern Italy, as well as *Paracrurithyris* sp. (Rhynchonellata) from South China, offering firm evidence for the pH trends presented in this study.

The effect of the dissociation constant for boric acid (pK_B^*) on the calculated pH is comparatively only very minor. For our pH calculation we used $pK_B^* = 8.60$, corresponding to the typical pre-event temperatures of about 25 °C and salinity of 35, based on our data as well as conodont-derived pre-event temperatures[6,30] and considering that the general Late Permian salinity[31,70] and major ion chemistry and mineralogy[70] was largely similar to present day conditions. We note that a temperature increase by 5 or 10 °C for example, would give a pK_B^* of 8.54 or 8.48, which would translate to a decrease in pH values by 0.06 and 0.12 units, respectively. This would only magnify the reported pH decline simultaneous with the major phase of warming,

although at such low pH range the pK_B^* influences on pH values would be largely within the uncertainties.

Model setup

A geochemical box model was set up to simulate the processes in the global ocean based on a recent ocean circulation model[8] for the PTB (see Supplement S4 for a detailed description of the model). Basin volumes, seafloor areas, and the water fluxes between the boxes employed in the model are taken from the circulation model (Extended Data Fig. 5). The recently developed redox-resolving biogeochemistry model REDBIO[25] was coupled to the box model to simulate the biogeochemical turnover in the ocean. REDBIO considers the following dissolved tracers: oxygen, nitrate, ammonium, phosphate, ferric iron, ferrous iron, total dissolved sulphide, dissolved inorganic carbon (^{12}C and ^{13}C) and total alkalinity. All tracer inventories change over time due to weathering inputs from land, CO_2 and O_2 fluxes across the ocean–atmosphere interface, nitrogen fixation, denitrification and redox-dependent fluxes at the seabed. Continental weathering and degassing fluxes, surface temperatures and atmospheric pCO_2 were simulated using the GEOCARB process formulations[72,73], whereas marine $\delta^{13}C$ values were calculated as described in a previous box model[74]. REDBIO was further extended to simulate the turnover of stable nitrogen isotopes in the ocean, considering total concentrations of dissolved nitrate and ammonium as well as the concentrations of ^{15}N-nitrate and ^{15}N-ammonium.

The model was run for a period of 2 Ma to reach a Late Permian equilibrium. Subsequently, a pulse of volcanic/metamorphic CO_2 was released to study the consequences of LIP degassing. The boundary parameters including the equilibrium climate sensitivity of 3 °C per doubling of pCO_2 were chosen based on the GEOCARB[75] models. Model results are shown on a timescale where the zero point is set at the onset of the negative carbon isotope excursion (CIE). The CO_2 flux induced by LIP degassing and its isotopic composition were varied systematically until the $\delta^{13}C$ of carbonates deposited on the continental shelf of the Tethys (see Supplement S4 for data sources) and the pH values in Tethys surface water were consistent with the available data (Fig. 2). Comparison of our model-derived atmospheric pCO_2 with previously published estimates[5] based on stomatal indices is available in Supplement (S5). Throughout the manuscript we use the terminology Tethys Ocean, which combines both Neotethys and Palaeotethys Oceans, since they are represented by a common box in the model.

Supplementary Information is available accompanying this contribution with further details on the stratigraphy and age model (S1), brachiopod samples (S2), analytical methods (S3), modelling (S4), and a comparison with stomatal pCO_2 estimates (S5).

Data availability

We have chosen not to deposit the data in a repository at this time but all geochemical data analysed during this study are accessible in the **Supplementary Data** file.

Code availability

Computer code is available upon reasonable request from K.W. (kwallmann@geomar.de).

References (only in Methods)

51. Posenato, R. Marine biotic events in the Lopingian succession and latest Permian extinction in the Southern Alps (Italy). *Geol. J.* **45**, 195−215 (2010).

52. Jurikova, H. *et al.* Boron isotope systematics of cultured brachiopods: response to acidification, vital effects and implications for palaeo-pH reconstruction. *Geochim. Cosmochim. Acta* **248**, 370–386 (2019a).

53. Broglio Loriga, C., Neri C., Pasini, M. & Posenato, R. Marine fossil assemblages from Upper Permian to lowermost Triassic in the western Dolomites (Italy). In: Cassinis, G. (Ed.) Permian and Permian–Triassic boundary in the South-Alpine segment of the western Tethys, and additional reports. *Memorie della Societa Geologica Italiana* **34**, 5–44 (1988).

54. Posenato, R. The athyridoids of the transitional beds between Bellerophon and Werfen formations (uppermost Permian, Southern Alps, Italy). *Riv. Ital. Paleontol. S.* **1071**, 197–226 (2001).

55. Kearsey, T., Twichett, R.J., Price, G.D. & Grimes, S.T. Isotope excursion and palaeotemperature estimates from the Permian/Triassic boundary in the Southern Alps (Italy). *Palaeogeogr. Palaeoclimatol. Palaeoecol.* **279**, 29–40 (2009).

56. Muttoni, G. *et al.* Opening of the Neo-Tethys Ocean and the Pangea B to Pangea A transformation during the Permian. *GeoArabia* **14**, 17–48.

57. Reichow, M.K. *et al.* The timing and extent of the eruption of the Siberian Traps large igneous province: Implications for the end-Permian environmental crisis. *Earth Planet. Sci. Lett.* **277**, 9–20 (2009).

58. Brand, U., Logan, A., Hiller N. & Richardson J. Geochemistry of modern brachiopods: applications and implications for oceanography and paleoceanography. *Chem. Geol.* **198**, 305–334 (2003).

59. Rollion-Bard, C. *et al.* Assessing the biomineralisation processes in the shell layers of modern brachiopods from oxygen isotopic composition and elemental ratios: Implications for their use as paleoenvironmental proxies. *Chem. Geol.*

524, 49−66 (2019).

60. Jurikova, H., *et al.* Incorporation of minor and trace elements into cultured brachiopods: Implications for proxy application with new insights from a biomineralisation model. *Geochim. Cosmochim. Acta* **286**, 418–440 (2020).

61. Jurikova, H. *et al.* Boron isotope composition of the cold-water coral *Lophelia pertusa* along the Norwegian margin: Zooming into a potential pH-proxy by combining bulk and high-resolution approaches. *Chem. Geol.* **513**, 143–152 (2019b).

62. Kasemann, S.A., S.A., Schmidt, D.N., Bijima, J. & Foster, G.L. *In situ* boron isotope analyses in marine carbonates and its application for foraminifera and palaeo-pH. *Chem. Geol.* **260**, 138–147 (2009).

63. Lemarchand, D., Gaillardet, J., Lewin, É. & Allègre, C. J. The influence of rivers on marine boron isotopes and implications for reconstructing past ocean pH. *Nature* **408**, 951–954 (2000).

64. Joachimski, M.M., Simon, L., van Geldern, R. & Lécuyer, C. Boron isotope geochemistry of Paleozoic brachiopod calcite: Implications for a secular change in the boron isotope geochemistry of seawater over the Phanerozoic. *Geochim. Cosmochim. Acta* **69**, 4035–4044 (2005)

65. Klochko, K., Kaufman, A.J., Wengsheng, Y., Byrne, R.H. & Tossell, J.A. Experimental measurement of boron isotope fractionation in seawater. *Earth Planet. Sci. Lett.* **248**, 276−285 (2006).

66. Lécuyer, C., Grandjean, P., Reynard, B., Albarède, F. & Telouk, P. $^{11}B/^{10}B$ analysis of geological materials by ICP-MS Plasma 54: application to the boron fractionation between brachiopod calcite and seawater. *Chem. Geol.* **186**, 45–55 (2002).

67. Ridgwell, A. A Mid Mesozoic Revolution in the regulation of ocean chemistry. *Mar. Chem.* **217**, 339–357 (2005)

68. Penman, D.E., Hönisch, B., Rasbury, E.T., Hemming, N.G., & Spero, H.J. Boron, carbon, and oxygen isotopic composition of brachiopod shells: Intra-shell variability, controls, and potential as a paleo-pH recorder. *Chem. Geol.* **340**, 32−39 (2013).

69. Garbelli, C., Angiolini, L., Brand, U. & Jadoul, F. Brachiopod fabric, classes and biogeochemistry: implications for the reconstruction and interpretation of seawater carbon-isotope curves and records. *Chem. Geol.* **371**, 60−67 (2014).

70. Khiel, J.T. & Shields, C.A. Climate simulations of the latest Permian: Implications for mass extinction. *Geology* **33**, 757–760 (2005).

71. Lowenstein, T.K., Timofeeff, M.N., Brennan, S.T., Hardie, L.A. & Demicco, R.V. Oscillations in Phanerozoic Seawater Chemistry: Evidence from Fluid Inclusions. *Science* **294**, 1086–1088 (2001).

72. Berner, R.A. & Kothavala, Z. GEOCARB III: A revised model of atmospheric CO_2 over Phanerozoic time. *Am. J. Sci.* **301**, 182−204 (2001).

73. Royer, D.L., Donnadieu, Y., Park, J., Kowalczyk, J. & Godderis, Y. Error analysis of CO_2 and O_2 estimates from the long-term geochemical model GEOCARBSULF. *Am. J. Sci.* **314**, 1259−1283 (2014).

74. Wallmann, K., Schneider, B. & Sarnthein, M. Effects of eustatic sea-level change, ocean dynamics, and nutrient utilization on atmospheric pCO_2 and seawater composition over the last 130,000 years. *Clim. Past.* **12**, 339–375 (2016).

75. Berner, R.A. GEOCARB II: A revised model of atmospheric CO_2 over Phanerozoic time. *Am. J. Sci.* **294**, 56–91 (1994).

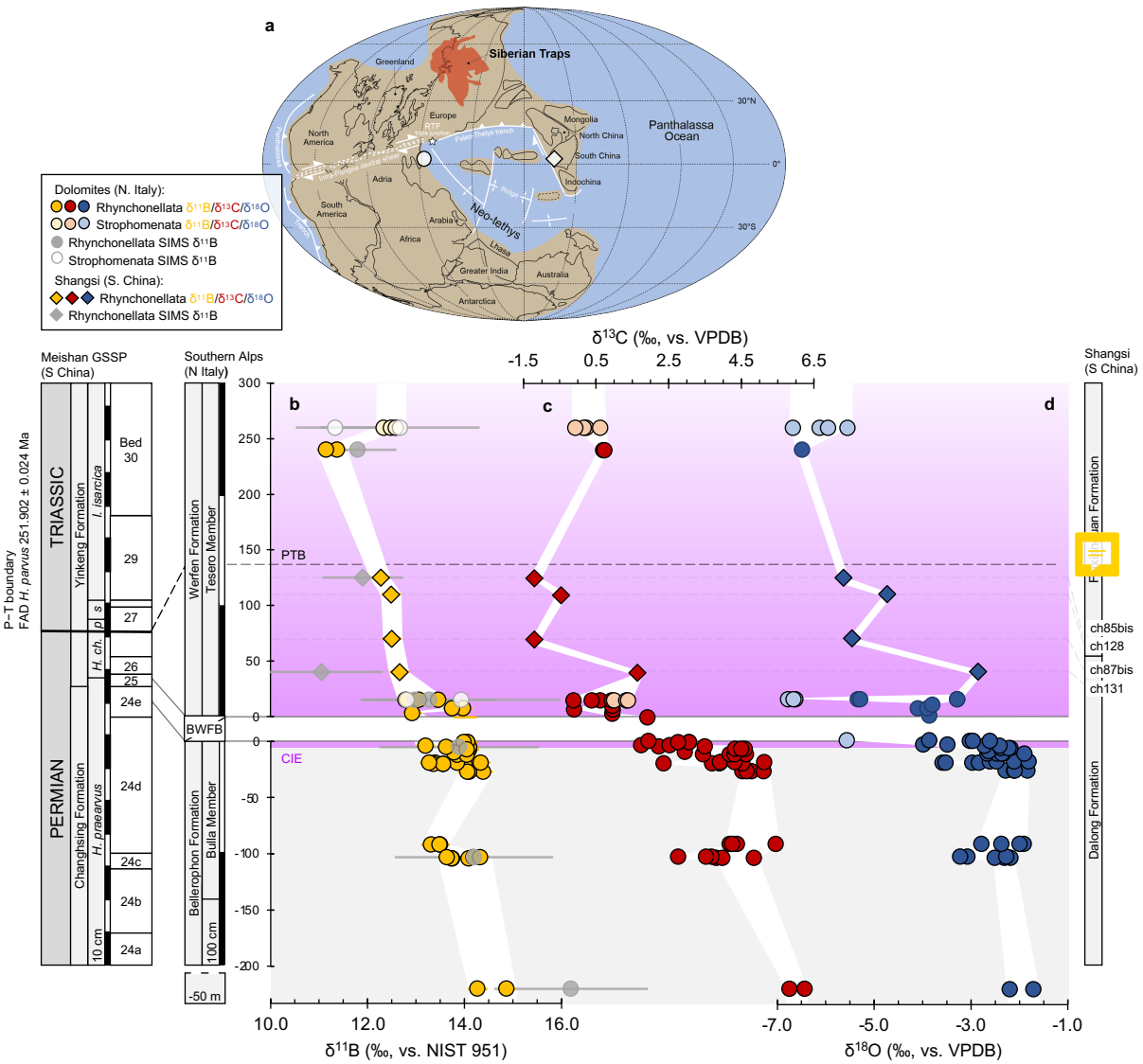
a
Siberian Traps
Greenland
Europe
North America
Mongolia
North China
South China
Indochina
Panthalassa Ocean
Adria
South America
Arabia
Africa
Neo-tethys
Lhasa
Greater India
Australia
Antarctica
30°N
0°
30°S
Dolomites (N. Italy):
Rhynchonellata δ11B/δ13C/δ18O
Strophomenata δ11B/δ13C/δ18O
Rhynchonellata SIMS δ11B
Strophomenata SIMS δ11B
Shangsi (S. China):
Rhynchonellata δ11B/δ13C/δ18O
Rhynchonellata SIMS δ11B
δ13C (‰, vs. VPDB)
-1.5
0.5
2.5
4.5
6.5
Meishan GSSP (S China)
Southern Alps (N Italy)
Shangsi (S China)
P–T boundary
FAD H. parvus 251.902 ± 0.024 Ma
TRIASSIC
PERMIAN
Yinkeng Formation
Changhsing Formation
I. isarcica
H. ch.
H. praearvus
Bed 30
29
27
26
25
24e
24d
24c
24b
24a
10 cm
Werfen Formation
Tesero Member
Bellerophon Formation
Bulla Member
100 cm
-50 m
BWFB
PTB
CIE
b
c
d
ch85bis
ch128
ch87bis
ch131
Dalong Formation
δ11B (‰, vs. NIST 951)
δ18O (‰, vs. VPDB)
10.0
12.0
14.0
16.0
-7.0
-5.0
-3.0
-1.0

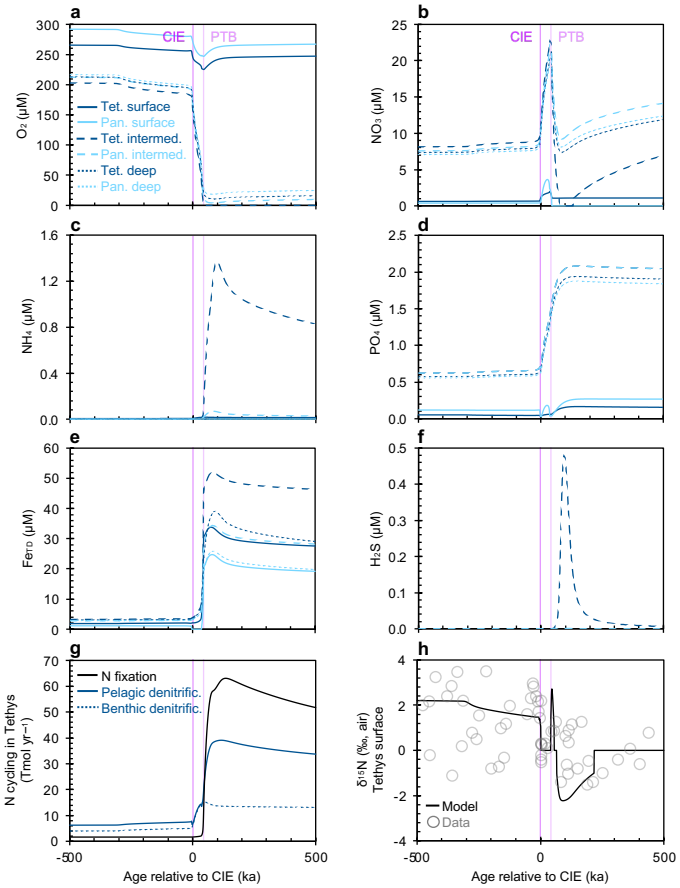
a
b
c
d
e
f
g
h
CIE
PTB
O2 (μM)
NO3 (μM)
NH4 (μM)
PO4 (μM)
FeTD (μM)
H2S (μM)
Tet. surface
Pan. surface
Tet. intermed.
Pan. intermed.
Tet. deep
Pan. deep
N fixation
Pelagic denitrific.
Benthic denitrific.
N cycling in Tethys (Tmol yr−1)
δ15N (‰, air) Tethys surface
Model
Data
Age relative to CIE (ka)

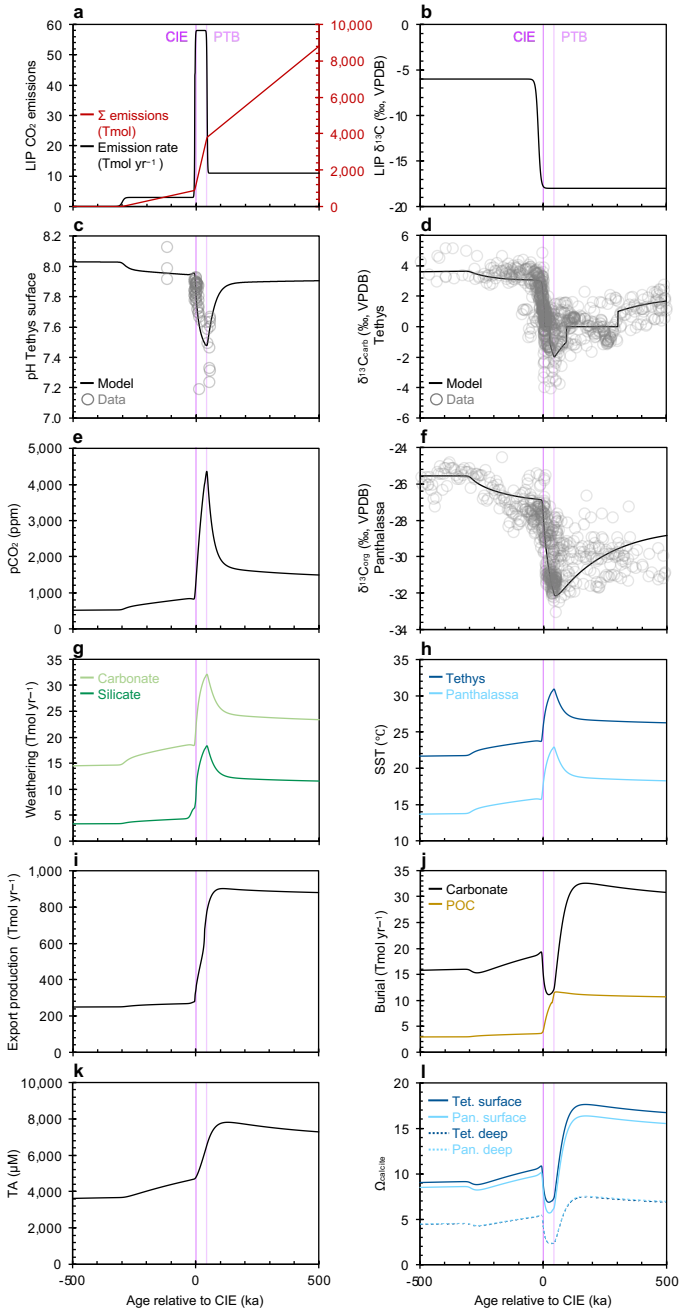
a
b
c
d
e
f
g
h
i
j
k
l
CIE
PTB
LIP CO2 emissions
Σ emissions (Tmol)
Emission rate (Tmol yr-1)
LIP δ13C (‰, VPDB)
pH Tethys surface
Model
Data
δ13Ccarb (‰ VPDB) Tethys
δ13Corg (‰ VPDB) Panthalassa
pCO2 (ppm)
Weathering (Tmol yr-1)
Carbonate
Silicate
SST (°C)
Tethys
Panthalassa
Export production (Tmol yr-1)
Burial (Tmol yr-1)
Carbonate
POC
TA (µM)
Ωcalcite
Tet. surface
Pan. surface
Tet. deep
Pan. deep
Age relative to CIE (ka)

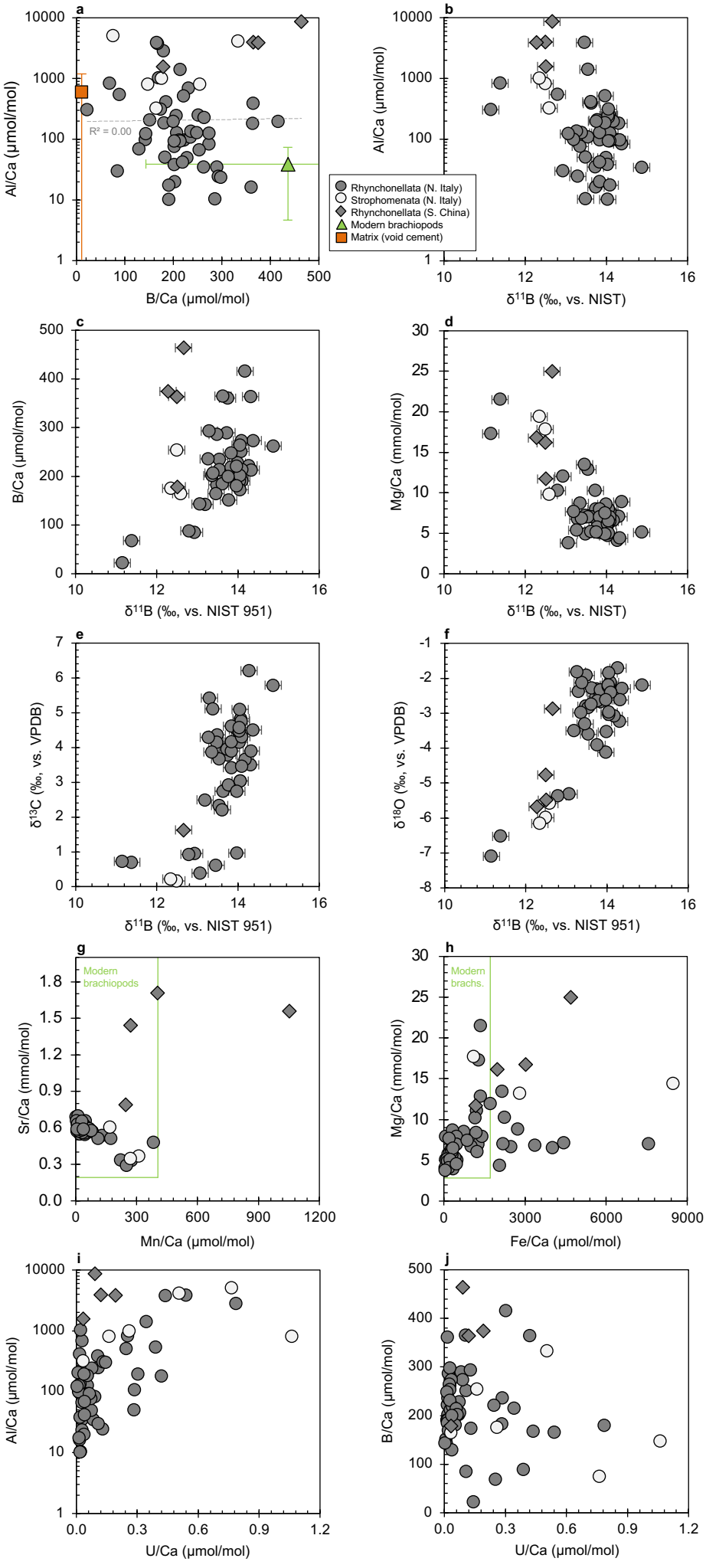
a
Al/Ca (µmol/mol)
B/Ca (µmol/mol)
R² = 0.00
Rhynchonellata (N. Italy)
Strophomenata (N. Italy)
Rhynchonellata (S. China)
Modern brachiopods
Matrix (void cement)
b
Al/Ca (µmol/mol)
δ11B (‰, vs. NIST)
c
B/Ca (µmol/mol)
δ11B (‰, vs. NIST 951)
d
Mg/Ca (mmol/mol)
δ11B (‰, vs. NIST)
e
δ13C (‰, vs. VPDB)
δ11B (‰, vs. NIST 951)
f
δ18O (‰, vs. VPDB)
δ11B (‰, vs. NIST 951)
g
Modern brachiopods
Sr/Ca (mmol/mol)
Mn/Ca (µmol/mol)
h
Modern brachs.
Mg/Ca (mmol/mol)
Fe/Ca (µmol/mol)
i
Al/Ca (µmol/mol)
U/Ca (µmol/mol)
j
B/Ca (µmol/mol)
U/Ca (µmol/mol)

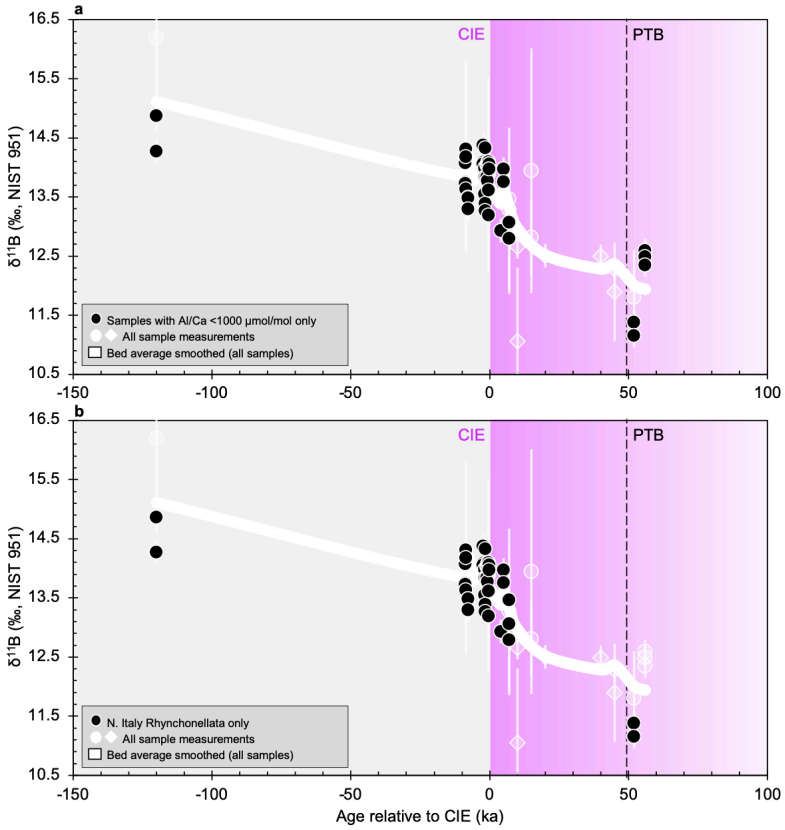
a
b
CIE
PTB
δ11B (‰, NIST 951)
16.5
15.5
14.5
13.5
12.5
11.5
10.5
-150
-100
-50
0
50
100
Samples with Al/Ca <1000 µmol/mol only
All sample measurements
Bed average smoothed (all samples)
N. Italy Rhynchonellata only
All sample measurements
Bed average smoothed (all samples)
Age relative to CIE (ka)

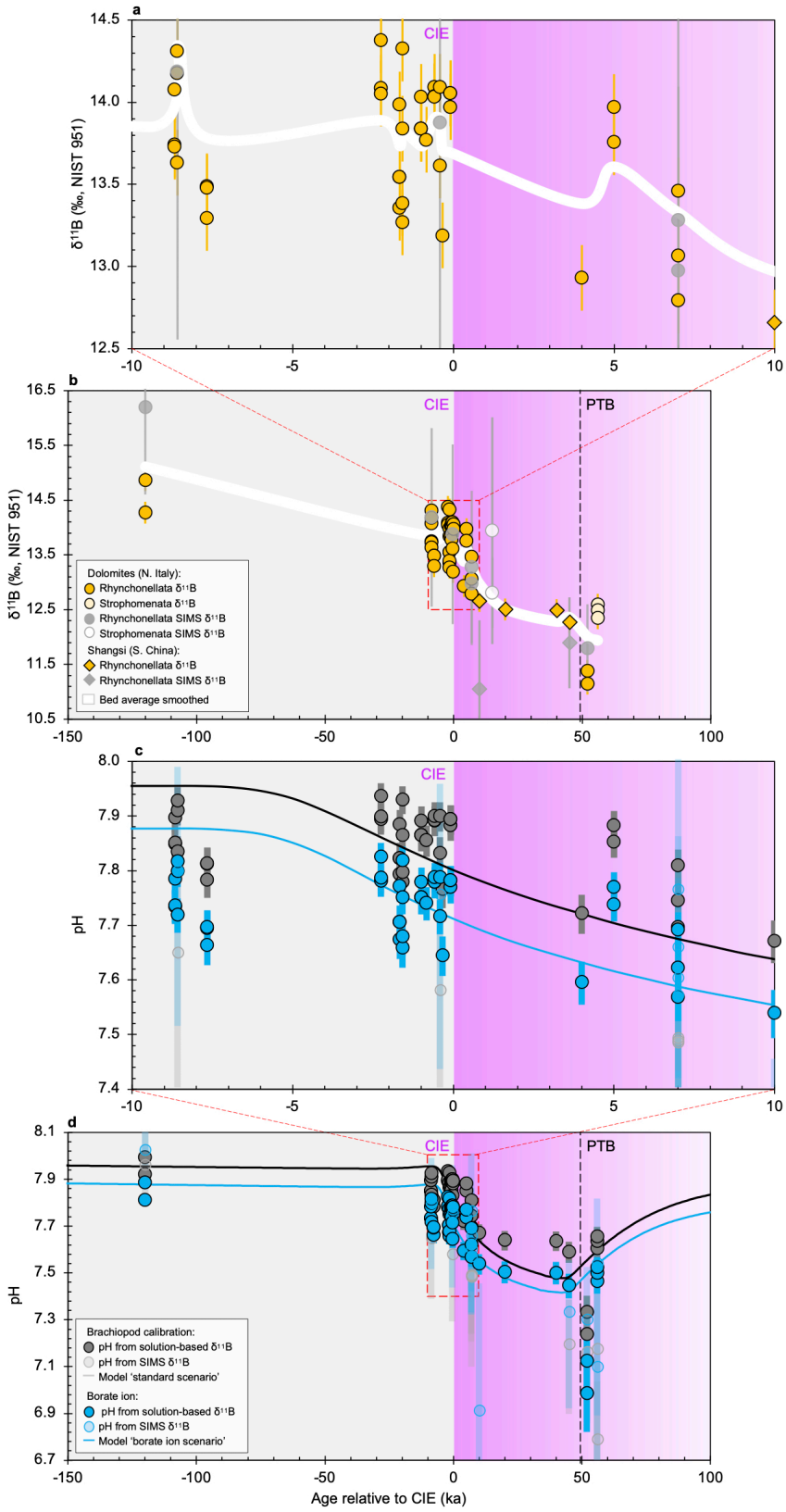
a
b
c
d
CIE
PTB
δ11B (‰, NIST 951)
pH
Age relative to CIE (ka)
Dolomites (N. Italy):
Rhynchonellata δ11B
Strophomenata δ11B
Rhynchonellata SIMS δ11B
Strophomenata SIMS δ11B
Shangsi (S. China):
Rhynchonellata δ11B
Rhynchonellata SIMS δ11B
Bed average smoothed
Brachiopod calibration:
pH from solution-based δ11B
pH from SIMS δ11B
Model 'standard scenario'
Borate ion:
pH from solution-based δ11B
pH from SIMS δ11B
Model 'borate ion scenario'

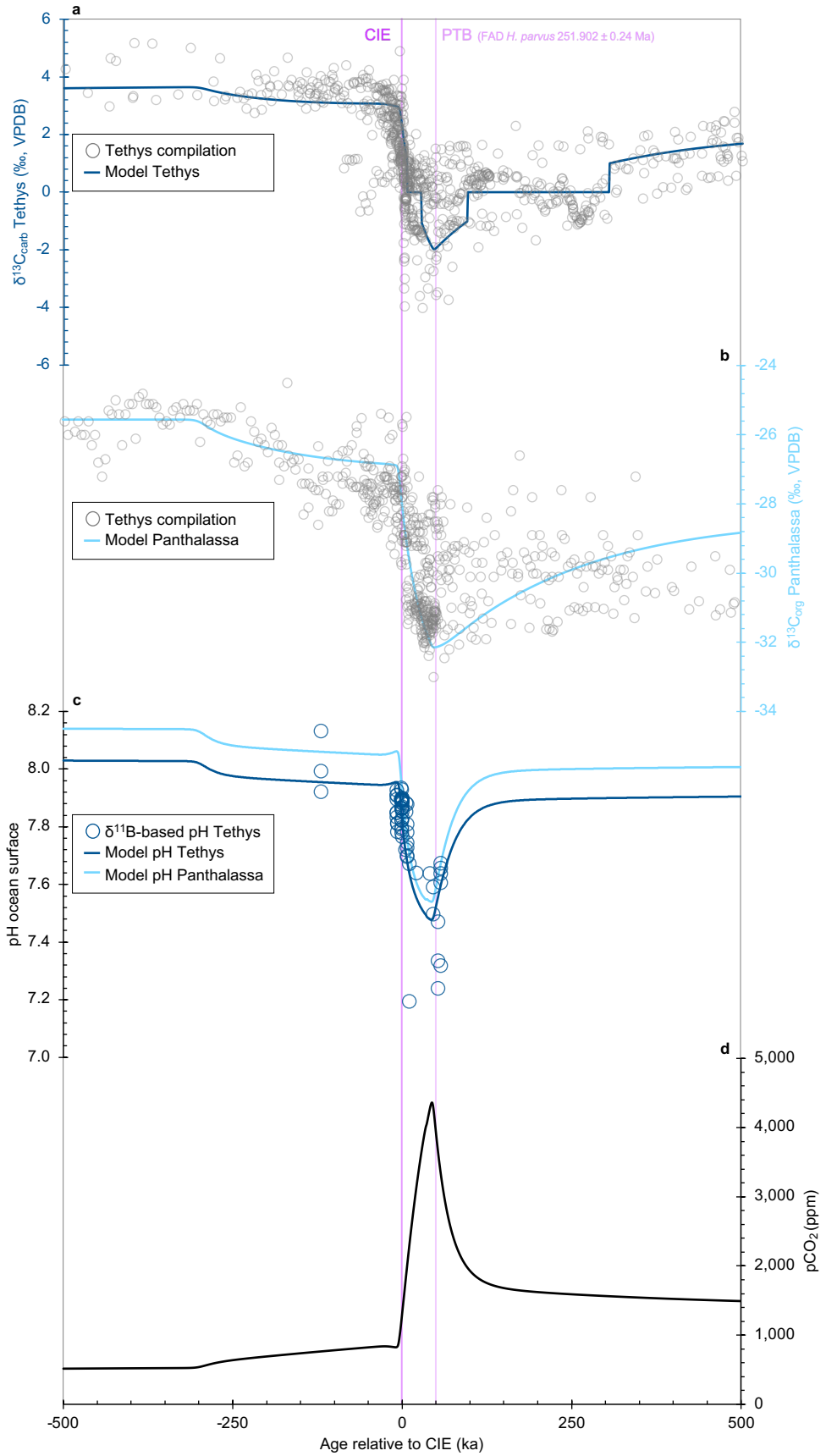
a
CIE
PTB (FAD H. parvus 251,902 ± 0.24 Ma)
Tethys compilation
Model Tethys
δ13Ccarb Tethys (‰, VPDB)
6
4
2
0
-2
-4
-6
b
Tethys compilation
Model Panthalassa
δ13Corg Panthalassa (‰, VPDB)
-24
-26
-28
-30
-32
-34
c
δ11B-based pH Tethys
Model pH Tethys
Model pH Panthalassa
pH ocean surface
8.2
8.0
7.8
7.6
7.4
7.2
7.0
d
pCO2 (ppm)
5,000
4,000
3,000
2,000
1,000
0
-500
-250
0
250
500
Age relative to CIE (ka)

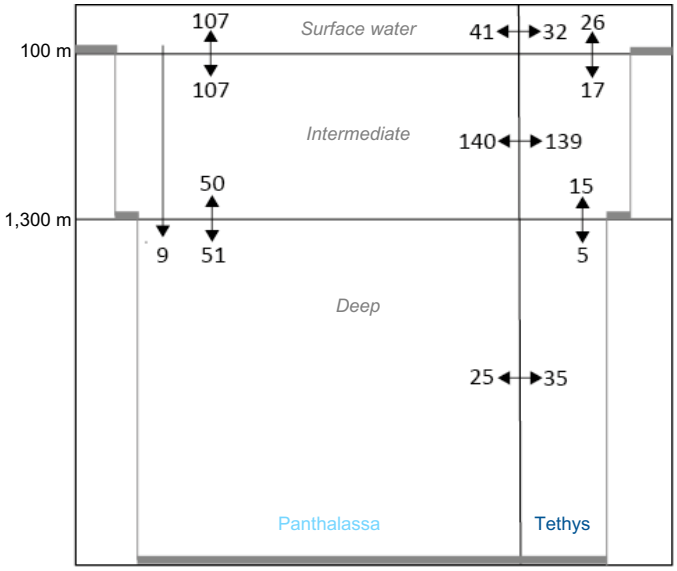
100 m
1,300 m
107
107
Surface water
41
32
26
17
Intermediate
140
139
50
51
9
15
5
Deep
25
35
Panthalassa
Tethys